

Unified neutron star equations of state calibrated to nuclear properties

Tuhin Malik*, Helena Pais**, and Constança Providência***

CFisUC, University of Coimbra, P-3004-516 Coimbra, Portugal.

Received xxx Accepted xxx

ABSTRACT

Context. Recently, in Malik et al. (2023), a dataset of several equations of state (EoS) for purely nucleonic stellar matter based on a non-linear relativistic-mean field (RMF) model prescription, and constrained to properties of nuclear matter, to state-of-the-art chiral effective field theory calculations for low-density neutron matter, and to astrophysical data, were proposed.

Aims. In this work, twenty one unified neutron star EoS were chosen from that dataset, in such a way that a large range of values of the slope of the symmetry energy at saturation is covered. Several quantities are calculated and discussed, such as the proton fraction and the direct Urca behavior, the density dependence of the speed of sound and the trace anomaly, the crust-core transition properties, the compatibility with astrophysical observations, and the neutron matter properties from chiral effective field theory (χ EFT) calculations and pQCD constraints.

Methods. We construct unified EoS, where the outer crust is given by the BSk22 functional, and the inner crust is calculated from a compressible liquid drop (CLD) approximation. The core is purely nucleonic, made of protons, neutrons, electrons and muons, under charge neutrality and in β -equilibrium conditions.

Results. The correlation of the slope of the symmetry energy at saturation with the crust-core transition density and proton fraction is analysed, and equations that translate these relations are proposed. Moreover, the spectral representation for all the EOS according to the format proposed in Lindblom (2010) is given, which is a convenient representation to study quasi-periodic oscillations with realistic EOS. It is shown that several of these EoS have in the center of the most massive NS a speed of sound squared of the order of $\lesssim 0.5$. Most of the EoS predict a maximum central density of the order of about 6 times the nuclear saturation density. Three of the EoS satisfy all of the constraints imposed. All these EoS will be made available in the CompOSE platform.

Key words. stars: neutron – equation of state – dense matter

1. Introduction

The macro and microscopic properties of neutron stars (NS) are still under study nowadays. However, with the present class of instrumentation, astrophysical measurements of both mass and radius of pulsars (Riley et al. 2019; Miller et al. 2019; Riley et al. 2021; Miller et al. 2021; Raaijmakers et al. 2021) and also the detection of gravitational wave signals from the merger of two NS, such as GW170817 (Abbott et al. 2017a) or the GW190425 (Abbott et al. 2020), have been possible, and this has allowed the nuclear physics community, working on the equation of state (EoS) for stellar matter, to further constraint their calculations. Microscopic calculations, such as *ab-initio* neutron matter calculations from χ EFT models (Hebeler et al. 2013; Drischler et al. 2019, 2020) have also been used to constraint the nuclear matter EoS in the low-density regime, i.e. at sub-saturation densities.

In the inner crust, heavy clusters (*nuclear pasta*) are expected to form due to the competition between the strong and Coulomb forces (Ravenhall et al. 1983). These geometries will have an effect on the transport properties and

cooling of the star, because of the possible modification of the neutrino mean-free path (Arcones et al. 2008). This layer of the star plays a big role in the determination of the radius of the star (see e.g Pais & Providência (2016) or Fortin et al. (2016)), since this quantity is affected by the determination of the crust-core transition. However, these nuclear clusters that form may pose a problem for its numerical calculation, so polytropic mechanisms to mimic the crust of the star, such as the one used in Carriere et al. (2003); Malik & Providência (2022), are often used.

Another quantity associated with the inner crust, and that has an effect, not only on R , but also on the slope of the symmetry energy, L , is the density at which the nuclear clusters melt, and the core, constituted by a homogeneous gas of protons, neutrons, and electrons and muons, starts. This is called the crust-core transition density, ρ_t . Previous studies (see e.g. Pais & Providência (2016); Ducoin et al. (2010); Newton et al. (2013); Providência et al. (2014)) have observed an anti-correlation between this quantity and L . Other studies have also tested other correlations (and combination of correlations) between nuclear matter parameters and EoS properties, such as ρ_t or the associated pressure, P_t (see e.g. Ducoin et al. (2011) or Alam et al. (2016)).

Besides the numerical computation of the inner crust, the lack of knowledge of the nuclear EoS at high densities

* tuhin.malik@uc.pt

** hpais@uc.pt

*** cp@uc.pt

together with the fact that the whole range of the star spans several orders of magnitude in density, makes the computation of a fully unified EoS a difficult task. Different prescriptions have been then proposed to contour this problem, such as metamodeling techniques (Margueron et al. 2018a,b; Ferreira et al. 2020; Xie & Li 2019, 2020; Ferreira & Providência 2021; Thi et al. 2021), that make a series expansion of the energy per nucleon to generate a realistic EoS, or non-parametric methods (Landry & Essick 2019; Essick et al. 2020; Gorda et al. 2022; Zhou et al. 2023), that infer the EoS directly from GW data. However, the composition is not determined within these kind of methods.

The density-dependence of the symmetry energy and its effect on the macroscopic properties of the star has been explored in several works (see e.g. Pais & Providência (2016); Cavagnoli et al. (2011); Providência & Rabhi (2013); Bao et al. (2014); Ji et al. (2019)), where relativistic mean-field models with non-linear meson terms have been used. In particular, the larger the Λ_ω parameter associated with the vector-isovector $\omega\rho$ mixing term is, the smaller the symmetry energy at saturation (Cavagnoli et al. 2011). Moreover, it has been shown that there exists a correlation between the non-linear vector meson ω term (ω^4 term) and the macroscopic properties of the star, such as the radius (Fattoyev & Piekarewicz 2010). This term seems to also affect the speed of sound, and a correlation between this term and the symmetry energy, has also been observed (Malik et al. 2023). The symmetry energy is known to play an important role in the composition of the star, and, consequently, on the nucleonic direct Urca processes (Yakovlev et al. 2001; Yakovlev & Pethick 2004; Fortin et al. 2020; Providência et al. 2019): if the symmetry energy is very low, very asymmetric matter is favoured and this will not allow for such kind of processes in the interior of NS (see e.g. Providência et al. (2023) and references therein).

The behaviour of the speed of sound has been also recently used to check when other, exotic, degrees of freedom set in, such as hyperons (Malik & Providência 2022), or even deconfined quark matter (Annala et al. 2020; Altirparmak et al. 2022; Somasundaram et al. 2022). Another quantity that has been used to test deconfinement is the trace anomaly, renormalized in Fujimoto et al. (2023) as $\Delta = 1/3 - P/\epsilon$, meaning that it should tend to zero in the conformal limit. In Annala et al. (2023), another related quantity was proposed, based also on the speed of sound, $d_c = \sqrt{\Delta^2 + \Delta'^2}$, where $\Delta' = c_s^2 (1/\gamma - 1)$ is the logarithmic derivative of Δ with respect to the energy density, which should also approach zero in the conformal limit.

In this work, we present 21 unified EOS based on the relativistic mean field approach used in Malik et al. (2023) including the constraints imposed in this work, and discuss their properties. The criterium to select the EOS is the slope of the symmetry energy at saturation, in particular, we consider values between 22 MeV and 70 MeV. The inner crust is built considering a compressible liquid drop approximation (Pais et al. 2015). Regarding the crust-core transition properties, we compare the values obtained from such a calculation with the ones obtained from a dynamical spinodal one (Pais & Providência 2016). Neutron star properties, such as the mass-radius curve, the tidal deformability, the crust-core transition density, the proton fraction, the speed of sound and the trace anomaly, among others, are given. A comparison between the performance of the different EOS

and the NS observations and the neutron matter EOS from a χ EFT calculation is discussed. We also give the spectral representation for all the EOS according to the format proposed in Lindblom (2010), which is a convenient representation to study quasi-periodic oscillations with realistic EOS. A discussion of the error introduced when the unified inner crust is not used, as in Malik et al. (2023), is also discussed.

2. Formalism

The twenty-one EoS are obtained within an RMF approach. The Lagrangian density that generates these models is written in terms of the fermionic fields that describe the nucleons, and the mesonic fields, the scalar isoscalar σ field, the vector isoscalar ω field, and the vector isovector ρ field, responsible for the description of the nuclear interaction. In the present formalism, non-linear meson terms are included to allow for a realistic modulation of the density dependence of both the symmetric nuclear matter and the symmetry energy. The role of these terms has been discussed in several seminal works Boguta & Bodmer (1977); Horowitz & Piekarewicz (2001); Mueller & Serot (1996); Sugahara & Toki (1994), and explored within a Bayesian inference study in Malik et al. (2023). The parameters are listed in Table 1.

2.1. The model

The Lagrangian describing the nuclear matter system is given by

$$\mathcal{L} = \mathcal{L}_N + \mathcal{L}_M + \mathcal{L}_{NL} \quad (1)$$

with

$$\begin{aligned} \mathcal{L}_N &= \bar{\Psi} \left[\gamma^\mu (i\partial_\mu - g_\omega \omega_\mu - g_\rho \mathbf{t} \cdot \boldsymbol{\rho}_\mu) \right. \\ &\quad \left. - (m - g_\sigma \sigma) \right] \Psi \\ \mathcal{L}_M &= \frac{1}{2} [\partial_\mu \sigma \partial^\mu \sigma - m_\sigma^2 \sigma^2] \\ &\quad - \frac{1}{4} F_{\mu\nu}^{(\omega)} F^{(\omega)\mu\nu} + \frac{1}{2} m_\omega^2 \omega_\mu \omega^\mu \\ &\quad - \frac{1}{4} F_{\mu\nu}^{(\rho)} \cdot \mathbf{F}^{(\rho)\mu\nu} + \frac{1}{2} m_\rho^2 \boldsymbol{\rho}_\mu \cdot \boldsymbol{\rho}^\mu. \\ \mathcal{L}_{NL} &= -\frac{1}{3} b m g_\sigma^3 (\sigma)^3 - \frac{1}{4} c g_\sigma^4 (\sigma)^4 + \frac{\xi}{4!} g_\omega^4 (\omega_\mu \omega^\mu)^2 \\ &\quad + \Lambda_\omega g_\rho^2 \boldsymbol{\rho}_\mu \cdot \boldsymbol{\rho}^\mu g_\omega^2 \omega_\mu \omega^\mu, \end{aligned}$$

where Ψ are the Dirac spinors that describe the nucleons, protons and neutrons, with a bare mass m . In the above expression, γ^μ are the Dirac matrices, \mathbf{t} is the isospin operator. We have introduced the following vector meson tensors $F^{(\omega,\rho)\mu\nu} = \partial^\mu A^{(\omega,\rho)\nu} - \partial^\nu A^{(\omega,\rho)\mu}$. The parameters g_σ , g_ω and g_ρ designate the couplings of the nucleons to the meson fields σ , ω and ρ with masses, respectively, m_σ , m_ω and m_ρ .

The coupling parameters of the non-linear terms b , c , ξ and Λ_ω together with the couplings g_i have been calculated imposing a set of constraints which will be next discussed. The role of the non-linear terms is briefly summarized: the non-linear σ terms introduced by Boguta & Bodmer (1977) control the nuclear matter incompressibility at saturation;

Table 1. The parameters for all 21 models obtained from the Lagrangian density 1. Specifically, B and C are $b \times 10^3$ and $c \times 10^3$, respectively. The nucleon, ω meson, σ meson, and ϱ meson masses considered are 939, 782.5, 500, and 763 MeV, respectively.

EOS	g_σ	g_ω	g_ρ	B	C	ξ	Λ_ω
EOS1	10.411847	13.219028	11.180337	2.541001	-3.586261	0.000845	0.027999
EOS2	10.485889	13.447123	9.640716	2.204058	-2.045914	0.015365	0.030662
EOS3	10.547924	13.478944	10.741298	2.345282	-2.397921	0.013874	0.034780
EOS4	10.764953	13.892817	16.316137	1.931926	-1.349144	0.017592	0.029602
EOS5	11.150279	14.420375	13.806001	2.036239	-1.635468	0.018019	0.037600
EOS6	8.027986	9.144665	13.334730	6.478531	-4.162544	0.001258	0.100686
EOS7	8.219347	9.263474	13.094357	7.304950	-4.472765	0.000789	0.089162
EOS8	8.637377	10.348224	11.228904	3.910898	-2.158740	0.001478	0.078386
EOS9	8.666023	10.123372	14.838137	5.068521	-3.068444	0.000005	0.072946
EOS10	8.674249	10.196514	14.188737	4.605767	-2.108763	0.000754	0.069895
EOS11	8.695491	10.431351	9.821776	3.975509	-2.615425	0.006394	0.039323
EOS12	8.720440	10.481072	12.378912	3.597999	-1.429640	0.002009	0.050647
EOS13	8.789344	10.482588	9.304529	4.597276	-4.641323	0.001198	0.031954
EOS14	8.885870	11.185655	11.060177	1.921115	-0.614536	0.006671	0.051142
EOS15	8.973194	10.876543	14.515228	3.783637	-3.414168	0.004491	0.055611
EOS16	9.123130	11.557699	11.708959	1.875115	-0.441126	0.012244	0.036703
EOS17	9.219420	11.126923	9.877649	4.039626	-4.268039	0.003467	0.035905
EOS18	9.220247	11.170082	11.087122	4.036904	-4.553914	0.003810	0.040742
EOS19	9.295923	11.527999	11.103228	3.135381	-3.390132	0.007847	0.039448
EOS20	9.554944	11.640795	14.692091	3.887915	-4.661381	0.003635	0.043001
EOS21	9.608190	11.957725	12.191950	3.117923	-4.098400	0.000255	0.058744

the ω^4 term was introduced in Sugahara & Toki (1994) and softens the EoS at high densities; the $\omega\rho$ term allows to control the density dependence of the symmetry energy. The meson-fields are taken as static, classical fields and replaced by their expectation values determined from the equations

$$\sigma = \frac{g_\sigma}{m_{\sigma,\text{eff}}^2} \sum_i \rho_i^s \quad (2)$$

$$\omega = \frac{g_\omega}{m_{\omega,\text{eff}}^2} \sum_i \rho_i \quad (3)$$

$$\varrho = \frac{g_\varrho}{m_{\varrho,\text{eff}}^2} \sum_i I_3 \rho_i, \quad (4)$$

with ρ_i^s and ρ_i , respectively, the scalar density and the number density of nucleon i , and

$$m_{\sigma,\text{eff}}^2 = m_\sigma^2 + b m g_\sigma^3 \sigma + c g_\sigma^4 \sigma^2 \quad (5)$$

$$m_{\omega,\text{eff}}^2 = m_\omega^2 + \frac{\xi}{3!} g_\omega^4 \omega^2 + 2\Lambda_\omega g_\omega^2 g_\varrho^2 \varrho^2 \quad (6)$$

$$m_{\varrho,\text{eff}}^2 = m_\varrho^2 + 2\Lambda_\omega g_\omega^2 g_\varrho^2 \omega^2. \quad (7)$$

In order to describe β -equilibrium matter, electrons and muons are introduced in the Lagrangian density

$$\mathcal{L}_l = \bar{\psi}_l \gamma^\mu (i\partial_\mu - m_l) \psi_l$$

Electric charge neutrality and β -equilibrium are imposed, defined by, respectively, the relations

$$\rho_p = \rho_e + \rho_\mu,$$

$$\mu_n = \mu_p + \mu_e, \quad \mu_\mu = \mu_e.$$

In order, to determine the NS properties, in particular, to integrate the Tolmann-Oppenheimer-Volkoff equations Tolman (1939); Oppenheimer & Volkoff (1939) to obtain the mass and radius of spherical static NS, the pressure and energy density must be calculated. The energy density is given by

$$\begin{aligned} \epsilon = & \sum_{i=n,p,e,\mu} \frac{1}{2\pi^2} \int_0^{k_{F_i}} \sqrt{k^2 + m_i^*} k^2 dk \\ & + \frac{1}{2} m_\sigma^2 \sigma^2 + \frac{1}{2} m_\omega^2 \omega^2 + \frac{1}{2} m_\varrho^2 \varrho^2 \\ & + \frac{b m}{3} (g_\sigma \sigma)^3 + \frac{c}{4} (g_\sigma \sigma)^4 + \frac{\xi}{8} (g_\omega \omega)^4 + 3\Lambda_\omega (g_\varrho g_\omega \varrho \omega)^2, \end{aligned} \quad (8)$$

where $m_i^* = m_i - g_\sigma \sigma$ for protons and neutrons and $m_i^* = m_i$ for electrons and muons, and k_{F_i} is the Fermi moment of particle i . The pressure is determined from the thermodynamic relation

$$P = \sum_i \mu_i \rho_i - \epsilon. \quad (9)$$

2.2. The outer crust

The outer crust region of the star is composed by a neutral lattice of nuclei and electrons. Even though there are several EoS in the literature for this layer of the star, in what concerns the macroscopic properties of the star, such as the mass and radius, the outer crust does not affect any of those, and, in principle, any EoS can be used. In the ComPOSE website, a public free online database collection of EoS for compact objects, we can find several of them. For this region, we chose the BSk22 EoS (Pearson et al. 2018),

taken from the CompOSE website (Typel et al. 2015; CompOSE Core Team et al. 2022; CompOSE 2024). This EoS was calculated using the Hartree-Fock-Bogoliubov atomic mass table HFB-22, and the 2016 Atomic Mass Evaluation (Audi et al. 2017), when the former masses were not available (see Fantina (2023) and references therein).

2.3. The inner crust

In the inner crust, heavy clusters are expected to form. Due to the competition between the strong and Coulomb forces, they form geometrical structures, being called the nuclear pasta phase due to their resemblance to the Italian food. These clusters may affect the cooling of the proton-neutron star, as the neutrino mean-free path may be affected, and they may also have consequence on the dynamics of the object, namely on the transport properties. Eventually these geometries will melt, and the core of the star is reached. This is denoted the crust-core transition.

In this work, this region of the star is calculated within the compressible liquid drop (CLD) model (Pais et al. 2015), considering β -equilibrium and zero temperature stellar matter. In this approximation, the system is composed of two distinct regions, the low-density one, denoted by II , i.e. the gas, composed of free neutrons, protons, and electrons, and the high-density one, denoted by I , the clusters. The total energy density of the system, the conditions for electrical neutrality, and β -equilibrium, are given respectively by

$$F = fF^I + (1-f)F^{II} + F_e + \varepsilon_{surf} + \varepsilon_{Coul}, \quad (10)$$

$$\rho_p = \rho_e + f\rho_p^I + (1-f)\rho_p^{II}, \quad (11)$$

$$\mu_n = \mu_p + \mu_e, \quad (12)$$

where $F^i, i = I, II$, is the free energy density of the homogeneous neutral nuclear matter, and the Coulomb and surface terms are given respectively by

$$\varepsilon_{Coul} = 2\alpha e^2 \pi \Phi R_d^2 (\rho_p^I - \rho_p^{II})^2, \quad (13)$$

$$\varepsilon_{surf} = \alpha D \sigma / R_d. \quad (14)$$

To find the stable solutions, the total energy is minimized against the variables of the system: the proton and neutron densities, in both phases, I and II , the radius of the geometry, r_d , and the fraction of phase I , f . From this minimization, we obtain the following equilibrium relations:

$$\begin{aligned} \varepsilon_{surf} &= 2\varepsilon_{coul}, \\ \mu_n^I &= \mu_n^{II}, \\ \mu_p^I &= \mu_p^{II} - \frac{2\varepsilon_{coul}}{f(1-f)(\rho_p^I - \rho_p^{II})}, \\ P^I &= P^{II} - \frac{2\varepsilon_{Coul}}{(\rho_p^I - \rho_p^{II})} \left(\frac{\rho_p^I}{f} + \frac{\rho_p^{II}}{(1-f)} \right) \\ &+ \varepsilon_{Coul} \left(\frac{3}{\alpha} \frac{\partial \alpha}{\partial f} + \frac{1}{\Phi} \frac{\partial \Phi}{\partial f} \right). \end{aligned} \quad (15)$$

with the radius of the geometry given by

$$R_d = \left(\frac{D\sigma}{4\pi e^2 \Phi (\rho_p^I - \rho_p^{II})^2} \right)^{1/3} \quad (16)$$

In these equations, $\alpha = f$ for droplets, rods, slabs and $\alpha = 1-f$ for tubes and bubbles, σ is the surface energy coefficient, D is the dimension of the geometry (3 for droplets), and Φ is given by

$$\Phi = \begin{cases} \left(\frac{2-D\alpha^{1-2/D}}{D-2} + \alpha \right) \frac{1}{D+2}, & D = 1, 3 \\ \frac{\alpha-1-\ln \alpha}{D+2}, & D = 2 \end{cases}. \quad (17)$$

3. Results

A collection of 21 equations of state based on Relativistic Mean Field (RMF) models, featuring a range of nuclear saturation properties, was created to explore the characteristics of neutron stars. The significance and implications of these 21 EOS models as well as their intricate properties will be discussed in the following.

A significant feature of neutron stars is their inner crust, which consists of non-homogeneous clustered matter, where we used a CLD calculation for the inner crust. Since this calculation is not fully self-consistent as the surface tension was chosen to be the same for all the models, we also perform a dynamical spinodal calculation to calculate the transition density. These two different approaches will be discussed in the following. In all the figures, we have highlighted the three EoS, EoS 8, 18, and 19, that have passed all the constraints discussed in Section 3.3.

3.1. Properties of the EoS

In Table 2, the properties of the 21 EOS are summarized. These include the nuclear matter parameters, defined from the usual approximation for the energy per nucleon

$$\varepsilon(\rho, \delta) \simeq \varepsilon(\rho, 0) + S(\rho)\delta^2, \quad (18)$$

where $\varepsilon(\rho, 0)$ is the symmetric nuclear matter (SNM) EOS, $S(\rho)$ is the the symmetry energy and $\delta = (\rho_p - \rho_n)/(\rho_p + \rho_n)$ is the asymmetry. The symmetric nuclear matter parameters defined at saturation are the energy per nucleon $\varepsilon_0 = \varepsilon(\rho_0, 0)$ ($n = 0$), the incompressibility coefficient K_0 ($n = 2$), the skewness Q_0 ($n = 3$), and the kurtosis Z_0 ($n = 4$), respectively, given by

$$X_0^{(n)} = 3^n \rho_0^n \left(\frac{\partial^n \varepsilon(\rho, 0)}{\partial \rho^n} \right)_{\rho_0}, \quad n = 2, 3, 4; \quad (19)$$

The symmetry energy parameters at saturation are: the symmetry energy at saturation $J_{\text{sym},0}$ ($n = 0$),

$$J_{\text{sym},0} = S(\rho_0) = \frac{1}{2} \left(\frac{\partial^2 \varepsilon(\rho, \delta)}{\partial \delta^2} \right)_{\delta=0}, \quad (20)$$

the slope $L_{\text{sym},0}$ ($n = 1$), the curvature $K_{\text{sym},0}$ ($n = 2$), the skewness $Q_{\text{sym},0}$ ($n = 3$), and the kurtosis $Z_{\text{sym},0}$ ($n = 4$), respectively, defined as

$$X_{\text{sym},0}^{(n)} = 3^n \rho_0^n \left(\frac{\partial^n S(\rho)}{\partial \rho^n} \right)_{\rho_0}, \quad n = 1, 2, 3, 4. \quad (21)$$

Looking at Table 2, the binding energy per nucleon, denoted as ϵ_0 , displays a median value of -16.16 MeV, with its values spanning from -16.40 MeV to -15.72 MeV. The incompressibility of nuclear matter, represented by K_0 , had a median of 233 MeV, and its value varies between 190

Table 2. The following nuclear saturation properties are listed for all EOS models: saturation density (fm^{-3}), binding energy per nucleon ϵ_0 , incompressibility of nuclear matter K_0 , skewness Q_0 , kurtosis Z_0 , symmetry energy $J_{\text{sym},0}$, slope $L_{\text{sym},0}$, curvature $K_{\text{sym},0}$, skewness $Q_{\text{sym},0}$ and kurtosis $Z_{\text{sym},0}$ of symmetry energy, all in MeV, are evaluated at nuclear saturation density ρ_0 . Furthermore, we list the transition density ρ_t (fm^{-3}), β -equilibrium pressure P_t ($\text{MeV}\cdot\text{fm}^{-3}$), and proton fraction y_p at the transition density calculated with both the CLD and dynamical spinodal approach.

model	ρ_0	ϵ_0	K_0	Q_0	Z_0	$J_{\text{sym},0}$	$L_{\text{sym},0}$	$K_{\text{sym},0}$	$Q_{\text{sym},0}$	$Z_{\text{sym},0}$	CLD			Dynamical spinodal		
											ρ_t	P_t	y_p	ρ_t	P_t	y_p
EOS1	0.155	-16.08	177	-74	18944	33	64	77	1741	-17088	0.0781	0.5446	0.0349	0.0773	0.5204	0.0341
EOS2	0.161	-16.11	206	279	12222	31	70	21	551	-13709	0.0672	0.3599	0.0225	0.0638	0.3028	0.0202
EOS3	0.163	-16.15	192	375	15288	32	66	59	552	-17990	0.0726	0.4173	0.0287	0.0765	0.4475	0.0290
EOS4	0.149	-16.11	209	87	8883	35	47	79	402	-16785	0.0944	0.4781	0.0673	0.0849	0.3202	0.0648
EOS5	0.154	-15.72	190	614	12505	32	60	98	-68	-14841	0.0726	0.3180	0.0407	0.0741	0.2959	0.0391
EOS6	0.169	-16.4	252	-451	2181	33	26	-68	1492	-18264	0.127	0.7313	0.0613	0.1182	0.5178	0.0615
EOS7	0.15	-15.67	231	-472	2195	32	28	-128	1653	-14718	0.1107	0.7956	0.0586	0.1041	0.6686	0.0572
EOS8	0.151	-15.99	267	-332	1654	29	36	-77	1210	-11321	0.0944	0.4704	0.0373	0.0958	0.4456	0.0363
EOS9	0.144	-16.28	254	-420	2066	33	22	-72	1601	-19302	0.1162	0.6369	0.0676	0.1048	0.4110	0.0687
EOS10	0.144	-16.33	262	-401	1766	32	25	-89	1606	-17661	0.1107	0.6291	0.0634	0.1018	0.4570	0.0626
EOS11	0.157	-16.24	260	-400	2173	32	57	-134	864	-2126	0.0835	0.5762	0.0303	0.0862	0.5999	0.0305
EOS12	0.147	-16.22	276	-330	1388	33	39	-137	1529	-11075	0.0998	0.7261	0.0528	0.0966	0.6449	0.0508
EOS13	0.156	-16.15	238	-423	3038	32	63	-124	632	173	0.0781	0.5144	0.0252	0.0799	0.5365	0.0256
EOS14	0.162	-16.18	316	-100	808	31	46	-59	1154	-12403	0.1053	0.5870	0.0407	0.1013	0.5183	0.0392
EOS15	0.153	-16.16	245	-388	2900	34	29	-33	1478	-19325	0.1162	0.6430	0.0654	0.1055	0.4299	0.0655
EOS16	0.157	-15.78	290	-211	1283	34	50	-87	1272	-12007	0.0998	0.7242	0.0479	0.0970	0.6518	0.0460
EOS17	0.152	-16.62	233	-470	3829	31	56	-107	978	-3122	0.0781	0.5039	0.0282	0.0799	0.5186	0.0283
EOS18	0.155	-16.31	221	-491	4260	32	49	-92	1388	-8841	0.0889	0.6671	0.0394	0.0875	0.6263	0.0381
EOS19	0.165	-16.24	230	-332	5616	33	53	-48	1332	-12465	0.0944	0.6914	0.0409	0.0934	0.6506	0.0396
EOS20	0.147	-16.18	199	-567	4651	34	32	-19	1628	-18997	0.1053	0.6606	0.0657	0.0976	0.5082	0.0649
EOS21	0.156	-16.12	216	-339	6785	29	42	55	1146	-14120	0.0944	0.3955	0.0388	0.0915	0.3400	0.0373

MeV and 290 MeV. The skewness of the data, indicated by Q_0 , had a median of -339 MeV, with an extensive range from -491 MeV to 375 MeV. Regarding the transition density, symbolized as ρ_t , the median was calculated at 0.0944 fm^{-3} , with its range stretching from 0.067 fm^{-3} to 0.127 fm^{-3} . Lastly, the nuclear saturation density, ρ_0 , shows a more consistent agreement among the EOS models, with a median of 0.155 fm^{-3} and values ranging from 0.144 fm^{-3} to 0.165 fm^{-3} .

3.2. Equation of state

In Figure 1, the EoS of all the 21 models considered in this work are shown: the pressure is plotted as a function of the energy density for homogeneous stellar matter, with an inner crust calculated in the CLD method. This figure highlights the crust part, where the first branch, up to $\epsilon \sim 10 \text{ MeV}\cdot\text{fm}^{-3}$, represents the BSk22 outer crust, and the following branch, up to $\epsilon \sim 100 \text{ MeV}\cdot\text{fm}^{-3}$, represents the inner crust, as the value $\sim 150 \text{ MeV}\cdot\text{fm}^{-3}$ roughly corresponds to the nuclear saturation density, 0.15 fm^{-3} . At the transition to the core, the EoS that has the lowest value of the pressure is EoS 5, with $P_t = 0.318 \text{ MeV}\cdot\text{fm}^{-3}$, and the one that has the highest value is EoS 7, with $P_t = 0.7956 \text{ MeV}\cdot\text{fm}^{-3}$. These values are written in the previous Table 2.

Fig. 2 illustrates the intricate relationship between the proton fraction and density within neutron stars. This is a

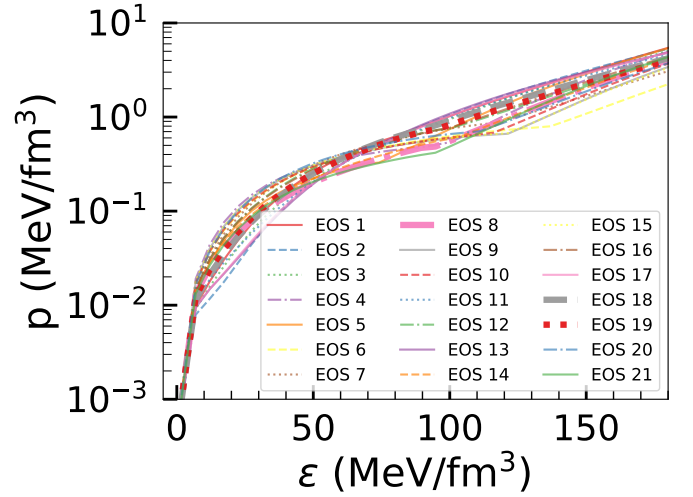


Fig. 1. Pressure versus energy density for neutron star matter in β -equilibrium, using our EOS set.

fundamental link to the symmetry energy of the model. The direct Urca (dUrca) threshold value of the proton fraction is particularly important. At this density the dUrca processes, a major factor in the cooling of NS, are triggered. The internal chemical composition of neutron stars (NS) is established through the weak interaction, specifically the β equilibrium condition. The composition has a major im-

pact on the cooling efficiency of both middle-aged isolated neutron stars and accreting neutron stars. The dUrca process, which involves the weak interaction-based conversion of neutrons into protons and vice versa, is much more efficient — approximately a million times — than the modified Urca process which occurs mediated by several nucleons, as highlighted in the research conducted by Yakovlev and collaborators Yakovlev et al. (2001); Yakovlev & Pethick (2004). The onset of the dUrca process requires a certain threshold in the proton fraction, specifically a minimum of $1/9$ if no muons or other charged species are considered, as pointed out by Lattimer et al. (1991). This threshold proton fraction increases slightly after the onset of muons. The proton fraction within neutron stars, denoted as y_p , increases with baryonic density. Therefore, in massive NSs, if y_p surpasses the critical threshold for the proton fraction, dUrca processes can potentially start. Recent studies, such as those by Beznogov & Yakovlev (2015), have used statistical approaches to describe the thermal evolution of isolated and accreting NSs. These studies suggest that a successful description of cooling curves is achievable by considering the onset of the dUrca processes in stars with masses of the order of 1.6 to 1.8 solar masses. Table 4 provides the dUrca threshold density ρ_{dUrca} and the corresponding NS mass M_{dUrca} for all models. Some models do not predict the occurrence of nucleonic dUrca in the NS interior. In this case, a slower, but still quite efficient process may occur if hyperons set in. Several models present the onset of the nucleonic dUrca inside stars with masses ~ 1.6 to $1.8 M_{\odot}$, but for most of the NS which allow nucleonic dUrca, it only occurs inside stars with a mass of the order of $2 M_{\odot}$ or larger. Notice, however, that if hyperonic degrees of freedom are allowed, hyperonic dUrca processes may occur inside NS with smaller masses, since the hyperonic dUrca processes open for densities close to the onset hyperon density.

Astrophysicists often opt for the functional form of the equation of state (EOS) instead of using tabulated data for computationally expensive calculations Abbott et al. (2018); Miller et al. (2019); Raaijmakers et al. (2020). We also present our 21 set of EOS in the spectral representation of realistic EOS, which offers a precise and efficient method to approximate any realistic EOS with an error of less than 0.5% Lindblom (2010). In Table 3, we show the parameters obtained from a spectral decomposition fit to the RMF EoS.

3.3. Constraints from the low-density regime

In this section, we analyse the symmetric nuclear matter and neutron matter properties of the 21 EoS, and compare with constraints available in the literature.

Figure 3 displays the pressure of pure neutron matter as a function of the baryon density for the 21 EOS we analyzed. We have included the theoretical constraints derived from state-of-the-art N3LO calculation within a χ EFT (dark grey), and the light grey represents the region where the uncertainty is doubled. All the equations of state in our dataset are affected by N3LO uncertainty.

If instead of considering the pure neutron matter pressure given in Hebeler et al. (2013), the pure neutron energy per particle obtained in Huth et al. (2022) is imposed with the given uncertainties, several EoS are completely out of the calculated range. This is shown in Figure 4, where the energy per neutron is plotted as a function of density, and

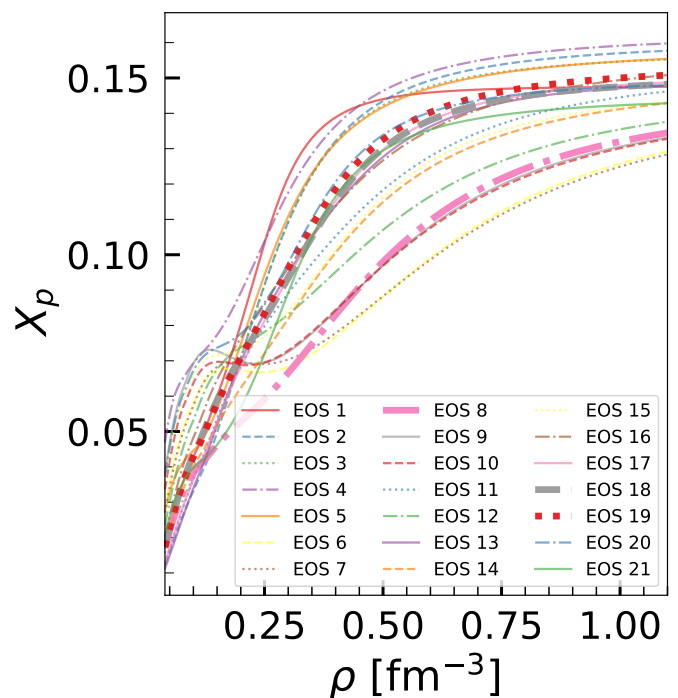


Fig. 2. The proton fraction as a function baryon density for all the twenty-one EOS considered.

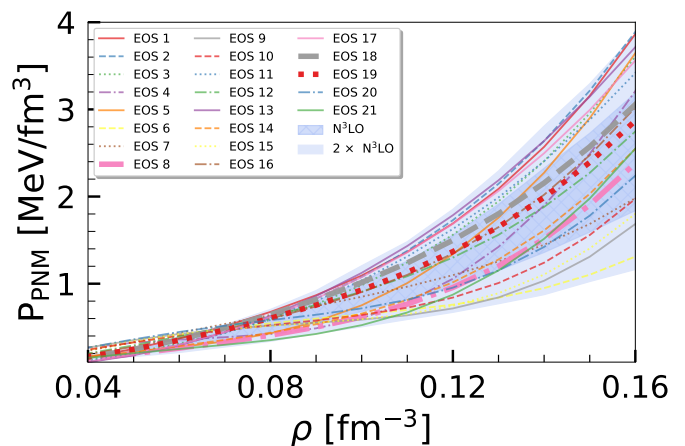


Fig. 3. Pure neutron matter pressure as a function of the baryonic density. The dark (light) blue band denotes the pure neutron matter calculated within a χ EFT description Hebeler et al. (2013) considering the uncertainty (twice the uncertainty) indicated.

compared with a band that corresponds to several χ EFT calculations: five EoS (EoS 1, 8, 18, 19 and 21) are inside the total density range 0.04 - 0.16 fm^{-3} , and 11 EoS are inside the range 0.08 - 0.16 fm^{-3} (see Table 7 at the end for a complete list of all satisfied constraints).

In Figure 5, the symmetry energy is shown and compared with the band extracted in Danielewicz & Lee (2014) from isobaric analog states (IAS). Twelve EoS satisfy this constraint, see Table 7 for a complete list.

3.4. Neutron star properties

In Figure 6, we show the mass-radius relations for all the models considered. In this figure several observational con-

Table 3. All the employed RMF EOS are converted to Spectral representation EOS format Lindblom (2010) in pressure based forms, where: $\epsilon_0/c^2 = 2.03 \times 10^{14}$ g/cm³ and $x_{max} = 10$. These are the parameters that have been fitted, along with the highest relative error, referred to as RE. The unit of p_0 is dyne \times cm⁻².

EOS	γ_0	γ_1	γ_2	γ_3	p_0	% RE
EOS1	0.9368	0.5084	-0.1512	0.0100	2.3e+33	0.5023
EOS2	0.6425	0.7209	-0.2287	0.0172	2.4e+33	0.0518
EOS3	0.6488	0.7571	-0.2360	0.0175	2.2e+33	0.0721
EOS4	1.0026	0.4939	-0.1660	0.0119	1.4e+33	0.0439
EOS5	0.8759	0.5776	-0.1959	0.0147	1.9e+33	0.0542
EOS6	1.1172	0.1133	-0.0317	0.0012	1.1e+33	0.0799
EOS7	1.1334	0.0755	-0.0249	0.0009	1.4e+33	0.0634
EOS8	1.2349	0.0871	-0.0326	0.0013	1.3e+33	0.1359
EOS9	1.3365	0.0650	-0.0342	0.0021	1.0e+33	0.2074
EOS10	1.4053	-0.0054	-0.0168	0.0007	1.1e+33	0.0948
EOS11	0.7885	0.3558	-0.0918	0.0048	2.2e+33	0.2113
EOS12	1.1019	0.1633	-0.0494	0.0023	1.6e+33	0.0668
EOS13	0.6199	0.5032	-0.1221	0.0071	2.5e+33	0.2778
EOS14	1.0968	0.2814	-0.0868	0.0049	1.3e+33	0.1851
EOS15	1.1175	0.2604	-0.0715	0.0034	1.0e+33	0.3341
EOS16	0.9500	0.3657	-0.1142	0.0073	1.7e+33	0.1548
EOS17	0.6207	0.5822	-0.1499	0.0091	2.3e+33	0.2642
EOS18	0.6025	0.6341	-0.1615	0.0098	2.0e+33	0.2765
EOS19	0.6244	0.6703	-0.1802	0.0115	1.8e+33	0.2340
EOS20	0.7339	0.6448	-0.1634	0.0097	1.2e+33	0.2055
EOS21	0.9125	0.5346	-0.1416	0.0088	1.2e+33	0.4828

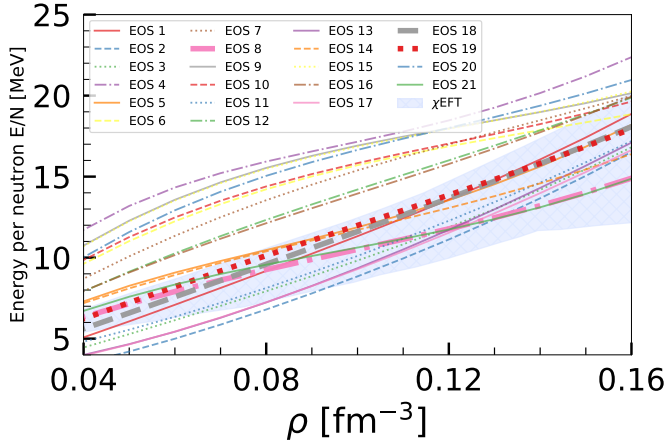


Fig. 4. Energy per neutron as a function of the baryonic density. The light blue band represents enclosed region of several χ EFT calculations taken from Huth et al. (2022)

straints are reported, as identified in the caption of Fig. 6. In particular, we conclude that all EoS satisfy the constraints from the gravitational wave event GW170817 at 90% CI, except EoS1. Also almost all EoS satisfy the constraints coming from NICER both for the PSR J0030 + 0451 and PSR J0740 + 6620 at 68% CI: only EoS6 does not fall inside the 1σ distribution obtained for PSR J0740 + 6620. We have also included the 1 and 2σ 2D distributions for the low mass compact object J1731-347 recently detected by the HESS (High Energy Stereoscopic System)

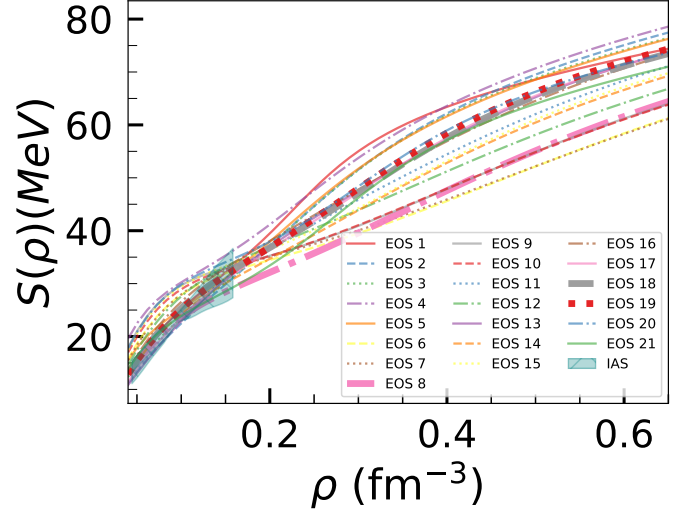


Fig. 5. The symmetry energy $S(\rho)$ as a function of density ρ for all the EOS. The constraints on the symmetry energy from IAS Danielewicz & Lee (2014) is also displayed.

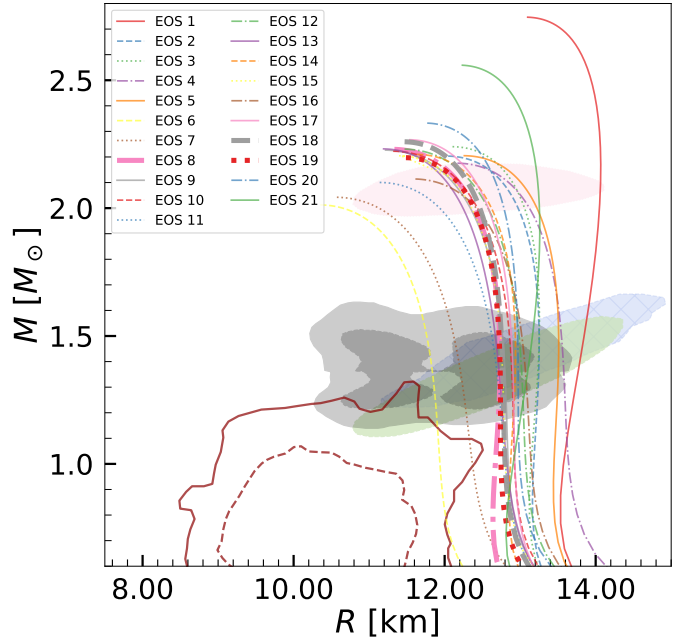


Fig. 6. NS mass-radius curves for all the twenty-one models with unified crust. The gray regions indicate the 90% (light) and 50% (dark) credible intervals (CI) constraints from the binary components of GW170817. The 1σ (68%) CI for the 2D posterior distribution in the mass-radii domain for the millisecond pulsar PSR J0030 + 0451 (cyan and green) Riley et al. (2019); Miller et al. (2019) as well as the PSR J0740 + 6620 (pink) Riley et al. (2021); Miller et al. (2021) from the NICER x-ray data are also shown. Additionally, we show the constraint obtained from HESS J1731-347 for 68.3% (95.4%) CIs in dashed dark red (solid dark red) Doroshenko et al. (2022).

collaboration. From all the EoS only EoS6 and EoS19 fall inside the 2σ CI.

The GW170817 event (Abbott et al. 2018) sets also constraints on the tidal deformability of stars with a mass of the order of $1.4M_{\odot}$. In Figs. 7 and 8, the combined tidal deformability and dimensionless tidal deformabilities are

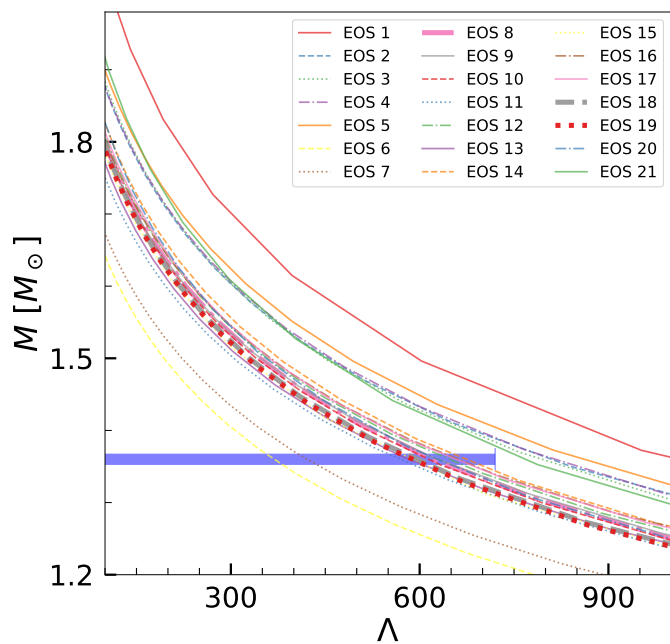


Fig. 7. The mass-tidal deformability relationship of neutron stars has been determined by taking into account all equations of state with a unified crust. The blue band indicates the tidal deformability for a mass ratio of $q = 1$ or for a neutron star of $1.36M_{\odot}$ that was part of the binary neutron star event GW170817 Abbott et al. (2018).

shown and compared with the values from the GW170817 event. The blue band in Fig. 7 identifies the constraint deduced from the tidal deformability of a $1.36M_{\odot}$ NS corresponding to the mass ratio of $q = 1$ between the masses of the binary NS, which within 90% CI is below 720. We conclude that only six EoS do not satisfy this constraint (EoS 1, 2, 3, 4, 5 and 21). In Fig. 8, the dimensionless tidal deformability parameters of both stars of the binary neutron star merger of the GW170817 event, Λ_1 and Λ_2 , are plotted for all the 21 RMF EoSs, taking into account the observed chirp mass $M_{\text{chirp}} = 1.186 M_{\odot}$, and compared with the data from the GW170817 event. The orange line (solid for 90% confidence and dashed for 50% confidence) indicates the confidence intervals obtained in Abbott et al. (2017b), while the blue shaded area highlights the marginalized posterior derived from a parameterized EoS imposing a maximum mass stipulation of $1.97 M_{\odot}$ by the LVC Abbott et al. (2019). Within the blue region, the solid and dashed lines depict 90% and 50% confidence intervals, respectively (see Abbott et al. (2019)). Considering the marginalized posterior at 90% CI only two EoS do not satisfy the constraints, EoS 1 and 5.

In Table 4, we summarize the NS properties of the 21 EoS, in particular we give the maximum mass M_{max} , the radius of the maximum mass star R_{max} , the radius for a 1.4 solar mass neutron star $R_{1.4}$, the radius for a 2.08 solar mass neutron star $R_{2.08}$, the dimensionless tidal deformability for a 1.4 solar mass neutron star $\Lambda_{1.4}$, the square of the speed of sound c_s^2 , the central baryonic density ρ_c , the dUrca onset density ρ_{dUrca} , and the NS mass where nucleonic dUrca processes open, M_{dUrca} . We conclude that except for EoS 1 and 21, all the EoS predict a central baryonic density $\rho_c \gtrsim 6\rho_0$. Concerning the speed of sound, five EoS predict $c_s^2 < 0.5$, ten EoS have $c_s^2 > 0.6$, but never above 0.8.

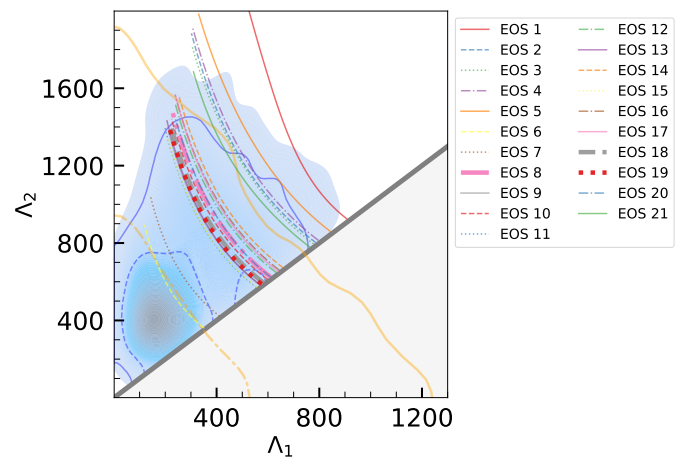


Fig. 8. The dimensionless tidal deformability parameters, denoted as Λ_1 and Λ_2 , are derived from the binary neutron star merger of the GW170817 event. These values are evaluated based on all 21 RMF EoSs, taking into account the observed chirp mass $M_{\text{chirp}} = 1.186 M_{\odot}$. The orange line (solid for 90% confidence and dashed for 50% confidence) indicates the confidence intervals, while the blue shaded area highlights the marginalized posterior derived from a parameterized EoS. This EoS has a maximum mass stipulation of $1.97 M_{\odot}$, and within this blue region, the solid and dashed lines again depict 90% and 50% confidence intervals, respectively.

3.5. Crust-core transition properties and correlations

In the present subsection we discuss some crust-core transition properties. We have considered two different calculations to determine the transition density: the CLD (Pais et al. 2015) and the dynamical spinodal (Pais & Providência 2016) calculation. In the first one we determine the non-homogeneous matter inside the inner crust considering for the heavy clusters a CLD description within a Wigner-Seitz approximation. In the second approach the transition density is defined by the zero eigenmode obtained when density fluctuations in infinite nuclear matter in β -equilibrium are considered. In Table 2, we show along with the saturation properties, the density, and correspondent pressure and proton fraction, at the crust-core transition, respectively ρ_t , P_t , $y_{p,t}$. In principle, if the calculation of the non-homogeneous matter had been carried out in a self-consistent calculation as the Thomas Fermi description in Avancini et al. (2010), we would expect the prediction from the dynamical spinodal to be slightly below the CLD one. However, the CLD calculation is not totally self-consistent due to the surface tension considered. There are six EoS for which the spinodal transition is above the CLD but the difference is $\lesssim 2\%$. The values predicted are of the order of $\rho_0/2 - 2\rho_0/3$, the smallest being $\sim 0.07\text{fm}^{-3}$ and the largest $\sim 0.13\text{fm}^{-3}$. At the transition, the pressure varies between ~ 0.35 and $0.70 \text{ MeV}/\text{fm}^3$. Another quantity that is also interesting is the proton fraction at the crust core transition. For the 21 EoS, it is generally above 0.03 (except for 3 EoS) and can be as high as 0.065. This is a quantity that is defining the behavior of the crust in the presence of a strong magnetic field as discussed in Fang et al. (2016, 2017); Wang et al. (2022): a low value of y_p may imply a larger inner crust.

In Ducoin et al. (2010, 2011), it was shown that the crust-core transition density is well correlated with the

Table 4. For all twenty-one EOS models, we list several properties of neutron stars, such as the maximum mass M_{\max} , maximum radius R_{\max} , radius for a 1.4 solar mass neutron star $R_{1.4}$, radius for a 2.08 solar mass neutron star $R_{2.08}$, the dimensionless tidal deformability for a 1.4 solar mass neutron star $\Lambda_{1.4}$, the square of the speed of sound c_s^2 , the central baryonic density ρ_c , the durca and M_{durca} .

EOS	M_{\max} [M_{\odot}]	R_{\max} [km]	$R_{1.4}$ [km]	$R_{2.08}$ [km]	$\Lambda_{1.4}$	c_s^2 [c^2]	ρ_c [fm^{-3}]	ρ_{dUrca} [fm^{-3}]	M_{dUrca} [M_{\odot}]
EOS1	2.74	13.03	13.78	14.04	844	0.713	0.683	0.366	2.06
EOS2	2.20	11.97	13.18	12.79	658	0.435	0.877	0.432	1.74
EOS3	2.24	12.06	13.19	12.91	654	0.444	0.856	0.437	1.80
EOS4	2.17	12.05	13.37	12.84	657	0.419	0.873	0.394	1.59
EOS5	2.20	12.16	13.36	13.00	709	0.414	0.849	0.443	1.83
EOS6	2.01	10.28	11.73	0.00	291	0.665	1.168
EOS7	2.04	10.51	12.14	0.00	341	0.675	1.129
EOS8	2.23	11.23	12.57	12.17	511	0.658	0.955
EOS9	2.23	11.13	12.67	12.12	473	0.731	0.975
EOS10	2.22	11.23	12.76	12.21	499	0.684	0.969
EOS11	2.10	11.08	12.55	11.53	462	0.543	1.025
EOS12	2.23	11.39	12.92	12.37	529	0.634	0.953	0.829	2.07
EOS13	2.23	11.11	12.60	12.04	474	0.689	0.982
EOS14	2.21	11.53	12.77	12.38	551	0.527	0.926	0.644	2.05
EOS15	2.20	11.31	12.66	12.15	467	0.577	0.956	0.981	...
EOS16	2.11	11.53	12.96	12.07	538	0.466	0.949	0.938	2.20
EOS17	2.27	11.45	12.78	12.40	534	0.603	0.929	0.660	2.01
EOS18	2.26	11.40	12.70	12.31	487	0.596	0.939	0.611	2.09
EOS19	2.20	11.41	12.65	12.20	481	0.519	0.949	0.606	2.07
EOS20	2.33	11.70	12.91	12.66	514	0.597	0.885	0.562	1.94
EOS21	2.56	12.13	12.95	13.14	638	0.767	0.791	0.551	2.08

slope of the symmetry energy at saturation $L_{\text{sym},0}$. Since the 21 EoS have been precisely chosen by the value of this parameter, the 21 EoS span a quite large range, $22 \leq L_{\text{sym},0} \leq 70$ MeV. In Figure 9, we plot the transition density, pressure and proton fraction, respectively, ρ_t , P_t and $y_{p,t}$ in terms of the symmetry energy slope $L_{\text{sym},0}$. As discussed in Ducoin et al. (2010, 2011), the transition density ρ_t is very well correlated with $L_{\text{sym},0}$. Also the proton fraction $y_{p,t}$ shows a quite good correlation with $L_{\text{sym},0}$, but not the pressure P_t .

In Table 5, we present a fit of these correlations in terms of the symmetry energy parameters $J_{\text{sym},0}$, $L_{\text{sym},0}$ (ρ_t and $y_{p,t}$). For the pressure we also consider the two higher order parameters $K_{\text{sym},0}$ and $Q_{\text{sym},0}$. The absolute Pearson correlation coefficient $r_{x,y}$ for each relationship is also listed, together with the relative mean square error (RMSE). The stronger correlations with the smallest RMSE are precisely the ones obtained for the transition density.

Before finishing this sub-section, we would like to comment the approximation implemented in Malik et al. (2023) for the inner crust. In that work, the BPS EoS was used for the outer crust, and for the inner crust, a polytropic EoS was used. It was matched to the core EoS at 0.04fm^{-3} . Although this density is well below the crust-core transition, it was considered that the error introduced considering the outer core EoS already above this density would be small, because the energy difference between the homogeneous matter EoS and the non-homogeneous EoS is small in this range of densities, see Avancini et al. (2008). In Table 6 we list the neutron star radius of stars with masses between 1.4 and 2.0 solar masses for the 21 EoS, using the unified crust (CLD approach, as described in section 2.3),

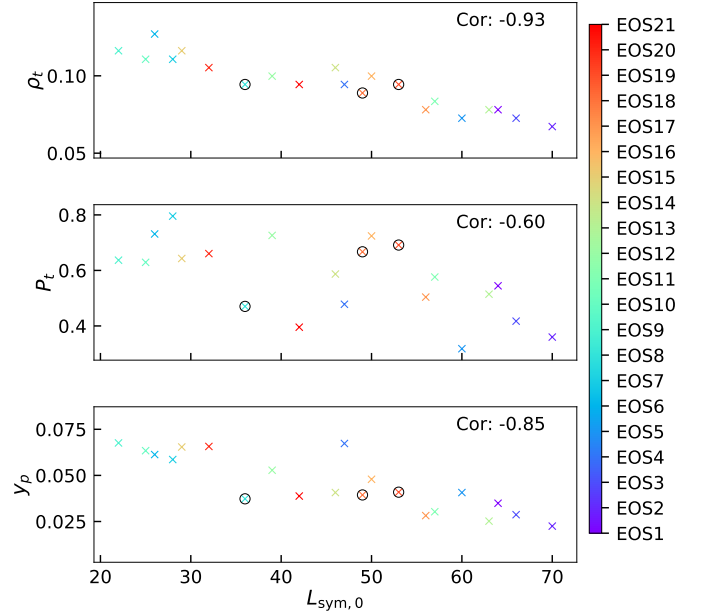


Fig. 9. From top to bottom, the figure illustrates the dependencies of the transition density (ρ_t), β -equilibrium pressure (p_t), and proton fraction (y_p) at core crust transition density over the symmetry energy slope parameter ($L_{\text{sym},0}$).

and the BPS + polytropic crust (as outlined in Malik et al. (2023)) as well as the corresponding percentage error. The maximum error introduced with the BPS + polytropic crust + core EoS at 0.04fm^{-3} is of the order of 1% - 1.5%, but in most cases it is well below 1%.

Table 5. Relations among core-crust transitional properties, i.e. the transition density ρ_t , and the β -equilibrium pressure P_t , and proton fraction $y_{p,t}$ at the transition density, with nuclear saturation properties. The absolute Pearson correlation coefficient $r_{x,y}$ for each relationship is also listed. Nuclear saturation properties are evaluated in MeV at saturation density $\rho_0 \text{ fm}^{-3}$. The units of ρ_t and P_t are fm^{-3} and $\text{MeV}\cdot\text{fm}^{-3}$, respectively. The proton fraction $y_{p,t}$ calculated at the transition density ρ_t is a dimensionless quantity. We also provide the average relative percentage of errors for each relation.

Quantity	Relations	abs($r_{x,y}$)	% Avg. RE
ρ_t	$\rho_t = -0.001 \times L_{\text{sym},0} + 0.1417$	0.93	4
	$\rho_t = \rho_0 (0.955 - 0.0075 \times L_{\text{sym},0})$	0.97	2.5
	$\rho_t = \rho_0 - 0.042 \times L_{\text{sym},0}/J_{\text{sym},0}$	0.98	2.7
P_t	$P_t = 0.0334 \times J_{\text{sym},0} - 0.00019 \times K_{\text{sym},0} + 0.00019 \times Q_{\text{sym},0} - 0.7246$	0.90	7.2
	$P_t = J_{\text{sym},0} \times (-2.2433\text{e-}5 \times K_{\text{sym},0} + 4.5913\text{e-}6 \times Q_{\text{sym},0} + 0.0117)$	0.93	7.9
y_p	$y_p = 0.0022 \times J_{\text{sym},0} - 0.0005 \times L_{\text{sym},0}$	0.95	11

Table 6. The neutron star radius for masses between 1.4 and 2.0 solar masses, using the unified crust (CLD approach, as described in section 2.3), and the BPS + polytropic crust (as outlined in Malik et al. (2023)), is listed here with the corresponding percentage error.

Model	With unified crust				with BPS + Polytropic crust				% error			
	$R_{1.4}$	$R_{1.6}$	$R_{1.8}$	$R_{2.0}$	$R_{1.4}$	$R_{1.6}$	$R_{1.8}$	$R_{2.0}$	$\Delta R_{1.4}$	$\Delta R_{1.6}$	$\Delta R_{1.8}$	$\Delta R_{2.0}$
EOS 1	13.79	13.9	13.99	14.05	13.78	13.88	13.97	14.03	0.07	0.14	0.14	0.14
EOS 2	13.25	13.24	13.17	12.97	13.18	13.18	13.11	12.92	0.53	0.45	0.46	0.39
EOS 3	13.24	13.25	13.21	13.06	13.19	13.2	13.16	13.01	0.38	0.38	0.38	0.38
EOS 4	13.57	13.51	13.39	13.12	13.37	13.34	13.24	13	1.47	1.26	1.12	0.91
EOS 5	13.51	13.5	13.42	13.22	13.36	13.37	13.31	13.13	1.11	0.96	0.82	0.68
EOS 6	11.82	11.69	11.42	10.65	11.73	11.61	11.36	10.59	0.76	0.68	0.53	0.56
EOS 7	12.19	12.03	11.76	11.13	12.14	11.99	11.72	11.09	0.41	0.33	0.34	0.36
EOS 8	12.74	12.71	12.61	12.39	12.57	12.57	12.5	12.29	1.33	1.1	0.87	0.81
EOS 9	12.79	12.73	12.6	12.34	12.67	12.63	12.51	12.26	0.94	0.79	0.71	0.65
EOS 10	12.88	12.82	12.69	12.44	12.76	12.72	12.6	12.36	0.93	0.78	0.71	0.64
EOS 11	12.68	12.56	12.36	11.93	12.55	12.45	12.27	11.86	1.03	0.88	0.73	0.59
EOS 12	13.01	12.95	12.82	12.57	12.92	12.87	12.75	12.51	0.69	0.62	0.55	0.48
EOS 13	12.71	12.63	12.49	12.24	12.6	12.53	12.4	12.17	0.87	0.79	0.72	0.57
EOS 14	12.94	12.92	12.83	12.62	12.77	12.78	12.71	12.52	1.31	1.08	0.94	0.79
EOS 15	12.76	12.71	12.6	12.36	12.66	12.62	12.52	12.29	0.78	0.71	0.63	0.57
EOS 16	13.06	12.97	12.8	12.42	12.96	12.88	12.72	12.35	0.77	0.69	0.63	0.56
EOS 17	12.9	12.86	12.76	12.58	12.78	12.76	12.68	12.5	0.93	0.78	0.63	0.64
EOS 18	12.77	12.73	12.64	12.47	12.7	12.67	12.59	12.42	0.55	0.47	0.4	0.4
EOS 19	12.73	12.7	12.6	12.39	12.65	12.63	12.54	12.33	0.63	0.55	0.48	0.48
EOS 20	12.97	12.96	12.91	12.78	12.91	12.9	12.85	12.73	0.46	0.46	0.46	0.39
EOS 21	13.12	13.2	13.25	13.26	12.95	13.06	13.13	13.14	1.3	1.06	0.91	0.9

3.6. Trace anomaly and speed of sound

The identification of a phase transition to deconfined matter inside NS has been the topic of many recent studies developed within different frameworks, see, for instance, Annala et al. (2020); Tews et al. (2018); Altiparmak et al. (2022); Gorda et al. (2022); Somasundaram et al. (2023, 2022). In Kurkela (2022), using a Gaussian Process description of the EoS, the authors have estimated which would be the effect of the EoS obtained in the perturbative QCD (pQCD) regime (i.e. above $\sim 40\rho_0$) on the EoS of neutron star matter. In particular, the authors have analysed the effect on the speed of sound.

In Fig. 10, we have plotted the speed of sound squared as a function of the baryonic density for our 21 EoS. In that figure, we also include the two regions calculated in Kurkela (2022) which define the 90% CI for the square of the speed of sound imposing only astrophysical constraints (the blue band denominated Astro) and astrophysical together with pQCD constraints (the brown band denominated Astro + pQCD). One of the consequences of imposing the pQCD constraints is to push the speed of sound to lower values at high densities and, in particular, to give raise to a peak at a baryonic density of the order of $\sim 0.5 \text{ fm}^{-3}$. The 21 EoS presented in our study are nucleonic EoS, without any kind of phase transition. No EoS shows a peak on the speed of

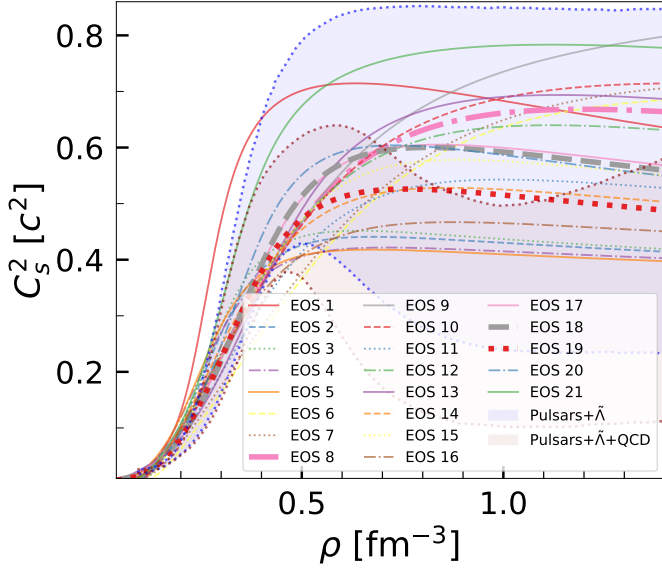


Fig. 10. The square of the speed of sound c_s^2 as a function of density for the EOS set considered. We also compare the posteriors obtained with "astro" and "astro" + pQCD constraint in Ref. Kurkela (2022).

sound at 0.5 fm^{-3} , but a large number flattens above this density, and some even stay inside the Astro + pQCD band for the whole range of densities, which may imply that the identification of the presence of a quark phase may be more difficult than expected.

Besides the speed of sound, other quantities have been proposed to identify the presence of quark matter inside NS: the polytropic index $\gamma = d \ln P / d \ln \epsilon$, where p is the pressure and ϵ is the energy density of the EoS (Annala et al. 2020), the trace anomaly $\Delta = 1/3 - P/\epsilon$ (Fujimoto et al. 2022), or a composition of these quantities, d_c , as defined in Annala et al. (2023). Within a pQCD calculation these quantities take the values $c_s^2 \lesssim 1/3$, $\gamma \in [1 : 1.7]$ and $\Delta \in [1 : 0.15]$ (Annala et al. 2023), at densities above $40\rho_0$. In the conformal limit $\gamma = 1$ and $\Delta = 0$.

Since these quantities can characterize properties of pure nucleonic EoS, built from a RMF description, we calculate them with the 21 EoS discussed in the present work. We have plotted c_s^2 , γ and Δ in Fig. 11 for all the EoS. We plot these quantities up to a density of the order of 1 fm^{-3} , which is approximately the central density of our maximum mass star, i.e. of stars with a mass M_{TOV} . At these densities, γ takes values between 1 and 1.5, and Δ may be slightly positive, but in general it takes negative values, that can be as low as -0.2, in agreement with the NS data plotted in Fig. 2 of Fujimoto et al. (2022) with results from Fujimoto et al. (2018, 2020).

Finally, in Fig. 12, we also plot the quantity proposed in Annala et al. (2023) as identifying the presence of quark matter, $d_c = \sqrt{\Delta^2 + \Delta'^2}$ with $\Delta' = c_s^2(1/\gamma - 1)$. $d_c = 0.2$ would represent the threshold limit for the presence of quark matter: $d_c > 0.2$ would imply purely hadronic matter while the $d_c < 0.2$ would imply only quark matter. While for some EoS, d_c stays well above 0.2, there are some for which in the center of the star $d_c < 0.2$. The idea is that Δ and Δ' should be small when γ and c_s^2 are close to the conformal limit. This would identify a phase transition to deconfined quark matter, which should have approximate

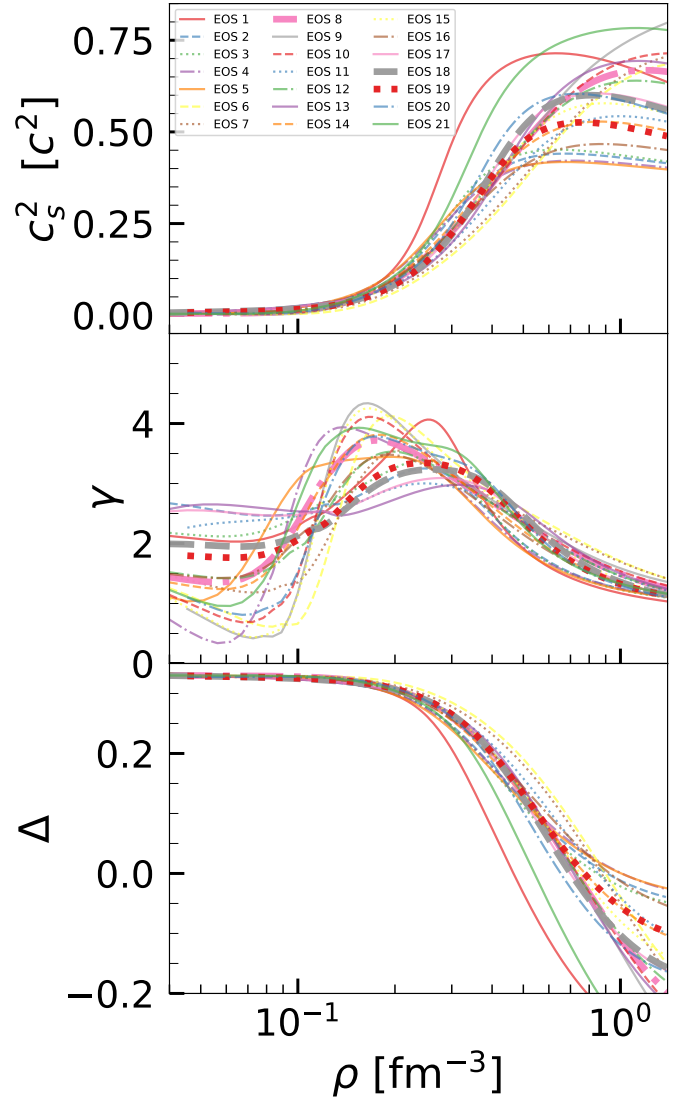


Fig. 11. The speed of sound squared c_s^2 , the polytropic index $\gamma = d \ln P / d \ln \epsilon$ and the trace anomaly $\Delta = 1/3 - P/\epsilon$ for all the EOS.

conformal symmetry. We are able to get small values for d_c because the polytropic index γ takes quite small values, even though the speed of sound square never comes below 0.4. The models that predict a small d_c are the ones with the smallest speed of sound square in the center of maximum mass star, $c_s^2 \lesssim 0.5$, and these are the models with the largest contribution from the ω^4 term, responsible for softening the EoS at high densities.

3.7. Discussion

In table 7 we summarize the behaviour of the 21 EoS with respect to several constraints that were discussed in previous subsections. These constraints include: the NS Mass-Radius from GW170817 within 50% CI and 90% CI, as well as the tidal deformability from the same event for mass ratio $q = 1$ or NS Mass $1.36 M_\odot$; symmetry energy constraints from IAS; pQCD constraints at $5 n_s$ and $7 n_s$ ($n_s = 0.16 \text{ fm}^{-3}$, and for renormalization scale $X = 2$) from Komoltsev & Kurkela (2022); pure neutron matter constraint derived from χ EFT calculations of the energy per particle from

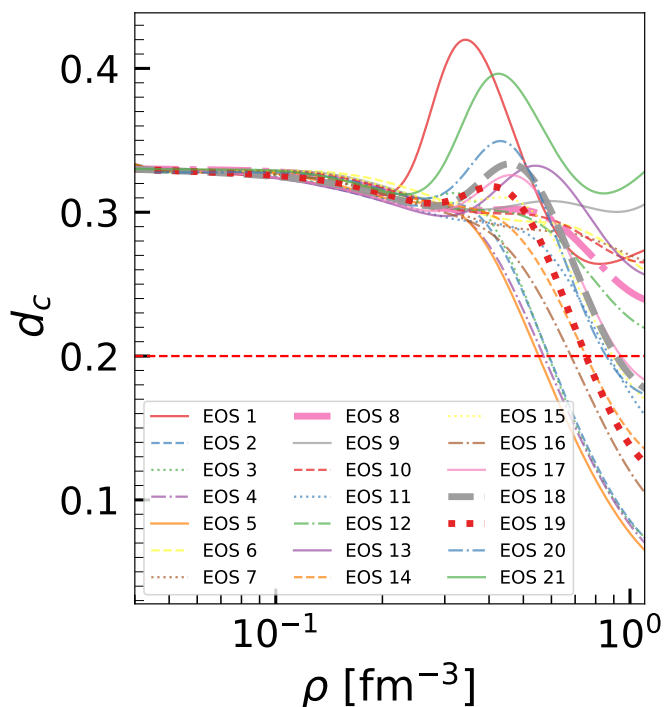


Fig. 12. This figure shows the relationship between d_c and ρ for all EoS (see text for details).

Huth et al. (2022) between $0.04\text{--}0.08\text{ fm}^{-3}$ and $0.08\text{--}0.16\text{ fm}^{-3}$ density. EoS that satisfy the criteria are indicated with right tick marks, and those that do not meet the criteria are marked with cross ticks in the table. Only EoS 8, 18 and 19 satisfy all constraints. EoS 11, 13, 14, and 17 just do not satisfy the χ EFT in the range $0.04\text{--}0.08\text{ fm}^{-3}$, and EoS 16 fails the χ EFT in all the ranges considered. EoS 6, 7, 9, 10, 12, 15 do not fall inside the E/N PNM envelop, and do not satisfy the IAS constraint. EoS 21 fails the tidal deformability and the pQCD at $7 n_s$ constraints.

4. Conclusions

We present twenty one EoS from the dataset generated in Malik et al. (2023), that has been constrained to a few properties of nuclear matter (binding energy at saturation, saturation density, incompressibility), the neutron matter pressure calculated within a χ EFT approach, and a minimum $2M_\odot$ NS maximum mass. The EoS were chosen in such a way that a large range of values of the slope of the symmetry energy at saturation is covered.

Unified inner-crust core EoS of β -equilibrium matter as expected inside neutron stars are built and several properties are discussed. The EoS satisfy the present available NS observations such as the ones from the GW170817 event Abbott et al. (2018), NICER observations of the pulsar PSR J0030 + 0451 Riley et al. (2019); Miller et al. (2019) and radio and NICER observation of pulsar PSR J0740 + 6620 Fonseca et al. (2021); Riley et al. (2021); Miller et al. (2021). It is shown that although constrained by the χ EFT pure neutron matter pressure calculations in the range $0.08\text{--}0.16\text{ fm}^{-3}$ only half of them satisfy the pure energy per particle χ EFT calculation of Huth et al. (2022) in the same range of densities, and not all these EoS satisfy simultaneously the IAS constraints proposed in Danielewicz & Lee (2014).

Special attention has been set on the determination of the crust-core transition and the matching of the crust to the core. We have analyzed the correlation of the slope of the symmetry energy at saturation with the crust-core transition density and proton fraction and proposed equations that translate these relations giving the corresponding absolute Pearson correlation coefficient.

Finally we have also discussed the behaviour of the speed of sound, trace anomaly and polytropic index, quantities frequently used to identify the possible existence of deconfined quark matter inside NS. It is shown that several of these EoS have in the center of the most massive NS a speed of sound squared of the order of $\lesssim 0.5$. Most of the EoS predict a maximum central density of the order of $6n_s$ with n_s a reference saturation density of nuclear matter. Only three of the EoS do not satisfy the pQCD constraints discussed in Komoltsev & Kurkela (2022) at $7n_s$.

Three of the EoS (8, 18 and 19) satisfy all the constraints discussed and four of them only fail the χ EFT in the range $0.04\text{--}0.08\text{ fm}^{-3}$ (EoS 11, 13, 14 and 17). The set that meets all the constraints is referred as UC Ia to UC Ic, and the one that fails only the lower part of the χ EFT PNM constraints is referred as UC IIa to UC II d, see table 7. The designation UC stands for Universidade de Coimbra. Notice that although the M-R curves of these seven EoS are similar, predicting similar NS properties, the high density properties and the NMP vary, and in particular, the larger values of the incompressibility are associated with smaller symmetry energy properties. EoS 16 fails the χ EFT in all the ranges of densities considered. Six EoS (6, 7, 9, 10, 12, and 15), besides failing the χ EFT constraint, also fail the IAS constraint in the complete range of densities given in Danielewicz & Lee (2014). EoS 21 only fails two constraints: the tidal deformability for NS having mass $1.36 M_\odot$ and pQCD at $7 n_s$.

5. Data Availability

All the calculated unified EOSs, together with their spectral fit for the inner core, will be available in the platform ComPOSE (2024).

ACKNOWLEDGMENTS

This work was partially supported by national funds from FCT (Fundação para a Ciência e a Tecnologia, I.P, Portugal) under projects UIDB/04564/2020 and UIDP/04564/2020, with DOI identifiers 10.54499/UIDB/04564/2020 and 10.54499/UIDP/04564/2020, respectively, and the project 2022.06460.PTDC with the associated DOI identifier 10.54499/2022.06460.PTDC. HP acknowledges the grant 2022.03966.CEECIND (FCT, Portugal) with DOI identifier 10.54499/2022.03966.CEECIND/CP1714/CT0004. The authors acknowledge the Laboratory for Advanced Computing at the University of Coimbra for providing HPC resources that have contributed to the research results reported within this paper, URL: <https://www.uc.pt/lca>.

References

- Abbott, B. P. et al. 2017a, Phys. Rev. Lett., 119, 161101
- Abbott, B. P. et al. 2017b, Astrophys. J. Lett., 848, L12
- Abbott, B. P. et al. 2018, Phys. Rev. Lett., 121, 161101

Table 7. List of each EOS satisfying constraints on NS Mass-Radius from GW170817 within 50% CI and 90% CI, tidal deformability for mass ratio $q = 1$ or for NS Mass $1.36 M_{\odot}$. Included are symmetry energy constraints from IAS, pQCD derived constraints at $5 n_s$ and $7 n_s$ ($n_s = 0.16 \text{ fm}^{-3}$, and the renormalization scale $X = 2$), and pure neutron matter constraint derived from χ EFT between $0.04\text{-}0.08 \text{ fm}^{-3}$ and $0.08\text{-}0.16 \text{ fm}^{-3}$. EOS that satisfy the criteria are indicated with right tick marks, and those that do not meet the criteria are marked with cross ticks in the table.

EOS	Named	M - R GW		$\Lambda_{1.36}$ GW	$S(\rho)$ IAS	pQCD X=2		E/N PNM envelop	
		50 CI	90 CI			5 ns	7 ns	$\rho = 0.04 - 0.08 \text{ fm}^{-3}$	$\rho = 0.08 - 0.16 \text{ fm}^{-3}$
EOS 1		X	X	X	✓	X	X	✓	✓
EOS 2		X	✓	X	✓	✓	✓	X	X
EOS 3		X	✓	X	✓	✓	✓	X	✓
EOS 4		X	✓	X	X	✓	✓	X	X
EOS 5		X	✓	X	X	✓	✓	X	✓
EOS 6		✓	✓	✓	X	✓	✓	X	X
EOS 7		✓	✓	✓	X	✓	✓	X	X
EOS 8	UCIa	✓	✓	✓	✓	✓	✓	✓	✓
EOS 9		✓	✓	✓	X	✓	✓	X	X
EOS 10		✓	✓	✓	X	✓	✓	X	X
EOS 11	UCIIa	✓	✓	✓	✓	✓	✓	X	✓
EOS 12		✓	✓	✓	X	✓	✓	X	X
EOS 13	UCIIb	✓	✓	✓	✓	✓	✓	X	✓
EOS 14	UCIIc	✓	✓	✓	✓	✓	✓	X	✓
EOS 15		✓	✓	✓	X	✓	✓	X	X
EOS 16		✓	✓	✓	✓	✓	✓	X	X
EOS 17	UCIIId	✓	✓	✓	✓	✓	✓	X	✓
EOS 18	UCIb	✓	✓	✓	✓	✓	✓	✓	✓
EOS 19	UCIc	✓	✓	✓	✓	✓	✓	✓	✓
EOS 20		✓	✓	✓	X	✓	X	X	X
EOS 21		✓	✓	X	✓	✓	X	✓	✓

- Abbott, B. P. et al. 2019, Phys. Rev. X, 9, 011001
 Abbott, B. P. et al. 2020, Astrophys. J. Lett., 892, L3
 Alam, N., Agrawal, B. K., Fortin, M., et al. 2016, Phys. Rev. C, 94, 052801
 Altiparmak, S., Ecker, C., & Rezzolla, L. 2022, Astrophys. J. Lett., 939, L34
 Annala, E., Gorda, T., Hirvonen, J., et al. 2023 [arXiv:2303.11356]
 Annala, E., Gorda, T., Kurkela, A., Nättilä, J., & Vuorinen, A. 2020, Nature Phys., 16, 907
 Arcones, A., Martínez-Pinedo, G., O'Connor, E., et al. 2008, Phys. Rev. C, 78, 015806
 Audi, G., Kondev, F., Meng, W., Huang, W., & Naimi, S. 2017, Chinese Physics C, 41, 030001
 Avancini, S. S., Chiacchiera, S., Menezes, D. P., & Providencia, C. 2010, Phys. Rev. C, 82, 055807, [Erratum: Phys.Rev.C 85, 059904 (2012)]
 Avancini, S. S., Menezes, D. P., Alloy, M. D., et al. 2008, Phys. Rev. C, 78, 015802
 Bao, S. S., Hu, J. N., Zhang, Z. W., & Shen, H. 2014, Phys. Rev. C, 90, 045802
 Beznogov, M. V. & Yakovlev, D. G. 2015, Mon. Not. Roy. Astron. Soc., 452, 540
 Boguta, J. & Bodmer, A. R. 1977, Nucl. Phys. A, 292, 413
 Carriere, J., Horowitz, C. J., & Piekarewicz, J. 2003, Astrophys. J., 593, 463
 Cavagnoli, R., Menezes, D. P., & Providencia, C. 2011, Phys. Rev. C, 84, 065810
 CompOSE. 2024, <https://compose.obspm.fr>
 CompOSE Core Team, Typel, S., Oertel, M., et al. 2022, European Physical Journal A, 58, 221
 Danielewicz, P. & Lee, J. 2014, Nucl. Phys. A, 922, 1
 Doroshenko, V., Suleimanov, V., Pühlhofer, G., & Santangelo, A. 2022, Nature Astronomy
 Drischler, C., Hebeler, K., & Schwenk, A. 2019, Phys. Rev. Lett., 122, 042501
 Drischler, C., Melendez, J. A., Furnstahl, R. J., & Phillips, D. R. 2020, Phys. Rev. C, 102, 054315
 Ducoin, C., Margueron, J., & Providencia, C. 2010, EPL, 91, 32001
 Ducoin, C., Margueron, J., Providencia, C., & Vidana, I. 2011, Phys. Rev. C, 83, 045810
 Essick, R., Landry, P., & Holz, D. E. 2020, Phys. Rev. D, 101, 063007
 Fang, J., Avancini, S., Pais, H., & Providencia, C. 2016, Phys. Rev. C, 94, 062801
 Fang, J., Pais, H., Pratapsi, S., et al. 2017, Phys. Rev. C, 95, 045802
 Fantina, A. 2023, <https://compose.obspm.fr/eos/256>
 Fattoyev, F. J. & Piekarewicz, J. 2010, Phys. Rev. C, 82, 025805
 Ferreira, M., Fortin, M., Malik, T., Agrawal, B. K., & Providencia, C. 2020, Phys. Rev. D, 101, 043021
 Ferreira, M. & Providencia, C. 2021, Phys. Rev. D, 104, 063006
 Fonseca, E. et al. 2021, Astrophys. J. Lett., 915, L12
 Fortin, M., Providencia, C., Raduta, A. R., et al. 2016, Phys. Rev. C, 94, 035804
 Fortin, M., Raduta, A. R., Avancini, S., & Providencia, C. 2020, Phys. Rev. D, 101, 034017
 Fujimoto, Y., Fukushima, K., Hotokezaka, K., & Kyutoku, K. 2023, Phys. Rev. Lett., 130, 091404
 Fujimoto, Y., Fukushima, K., McLerran, L. D., & Praszalowicz, M. 2022, Phys. Rev. Lett., 129, 252702
 Fujimoto, Y., Fukushima, K., & Murase, K. 2018, Phys. Rev. D, 98, 023019
 Fujimoto, Y., Fukushima, K., & Murase, K. 2020, Phys. Rev. D, 101, 054016
 Gorda, T., Komoltsev, O., & Kurkela, A. 2022 [arXiv:2204.11877]
 Hebeler, K., Lattimer, J. M., Pethick, C. J., & Schwenk, A. 2013, Astrophys. J., 773, 11
 Horowitz, C. J. & Piekarewicz, J. 2001, Phys. Rev. Lett., 86, 5647
 Huth, S., Pang, P. T. H., Tews, I., et al. 2022, Nature, 606, 276

- Ji, F., Hu, J., Bao, S., & Shen, H. 2019, *Phys. Rev. C*, 100, 045801
- Komoltsev, O. & Kurkela, A. 2022, *Phys. Rev. Lett.*, 128, 202701
- Kurkela, A. 2022, *EPJ Web Conf.*, 274, 07008
- Landry, P. & Essick, R. 2019, *Phys. Rev. D*, 99, 084049
- Lattimer, J. M., Prakash, M., Pethick, C. J., & Haensel, P. 1991, *Phys. Rev. Lett.*, 66, 2701
- Lindblom, L. 2010, *Phys. Rev. D*, 82, 103011
- Malik, T., Ferreira, M., Albino, M. B., & Providência, C. 2023, *Phys. Rev. D*, 107, 103018
- Malik, T. & Providência, C. 2022, *Phys. Rev. D*, 106, 063024
- Margueron, J., Hoffmann Casali, R., & Gulminelli, F. 2018a, *Phys. Rev. C*, 97, 025805
- Margueron, J., Hoffmann Casali, R., & Gulminelli, F. 2018b, *Phys. Rev. C*, 97, 025806
- Miller, M. C. et al. 2019, *Astrophys. J. Lett.*, 887, L24
- Miller, M. C. et al. 2021, *Astrophys. J. Lett.*, 918, L28
- Mueller, H. & Serot, B. D. 1996, *Nucl. Phys. A*, 606, 508
- Newton, W. G., Gearheart, M., & Li, B.-A. 2013, *Astrophys. J. Suppl.*, 204, 9
- Oppenheimer, J. R. & Volkoff, G. M. 1939, *Phys. Rev.*, 55, 374
- Pais, H., Chiacchiera, S., & Providência, C. 2015, *Phys. Rev. C*, 91, 055801
- Pais, H. & Providência, C. 2016, *Phys. Rev. C*, 94, 015808
- Pearson, J. M., Chamel, N., Potekhin, A. Y., et al. 2018, *Mon. Not. Roy. Astron. Soc.*, 481, 2994, [Erratum: *Mon. Not. Roy. Astron. Soc.* 486, 768 (2019)]
- Providência, C., Avancini, S. S., Cavagnoli, R., et al. 2014, *Eur. Phys. J. A*, 50, 44
- Providência, C., Malik, T., Albino, M. B., & Ferreira, M. 2023 [arXiv:2307.05086]
- Providencia, C. & Rabhi, A. 2013, *Phys. Rev. C*, 87, 055801
- Providência, C., Fortin, M., Pais, H., & Rabhi, A. 2019, *Frontiers in Astronomy and Space Sciences*, 6
- Raaijmakers, G., Greif, S. K., Hebel, K., et al. 2021, *Astrophys. J. Lett.*, 918, L29
- Raaijmakers, G. et al. 2020, *Astrophys. J. Lett.*, 893, L21
- Ravenhall, D. G., Pethick, C. J., & Wilson, J. R. 1983, *Phys. Rev. Lett.*, 50, 2066
- Riley, T. E. et al. 2019, *Astrophys. J. Lett.*, 887, L21
- Riley, T. E. et al. 2021, *Astrophys. J. Lett.*, 918, L27
- Somasundaram, R., Tews, I., & Margueron, J. 2022 [arXiv:2204.14039]
- Somasundaram, R., Tews, I., & Margueron, J. 2023, *Phys. Rev. C*, 107, 025801
- Sugahara, Y. & Toki, H. 1994, *Nucl. Phys. A*, 579, 557
- Tews, I., Carlson, J., Gandolfi, S., & Reddy, S. 2018, *Astrophys. J.*, 860, 149
- Thi, H. D., Mondal, C., & Gulminelli, F. 2021, *Universe*, 7, 373
- Tolman, R. C. 1939, *Phys. Rev.*, 55, 364
- Typel, S., Oertel, M., & Klähn, T. 2015, *Phys. Part. Nucl.*, 46, 633
- Wang, X., Li, J., Fang, J., Pais, H., & Providência, C. 2022, *Phys. Rev. D*, 105, 063004
- Xie, W.-J. & Li, B.-A. 2019, *Astrophys. J.*, 883, 174
- Xie, W.-J. & Li, B.-A. 2020, *Astrophys. J.*, 899, 4
- Yakovlev, D. G., Kaminker, A. D., Gnedin, O. Y., & Haensel, P. 2001, *Phys. Rept.*, 354, 1
- Yakovlev, D. G. & Pethick, C. J. 2004, *Ann. Rev. Astron. Astrophys.*, 42, 169
- Zhou, W., Hu, J., Zhang, Y., & Shen, H. 2023, *Astrophys. J.*, 950, 186